TOPOGRAPHICAL LENGTH SCALES OF HIERARCHICAL SUPERHYDROPHOBIC SURFACES

P. K. Dhillon[1], P. S. Brown[2], C. D. Bain[2], J. P. S. Badyal[2†], and S. Sarkar[1†*]

[1]Department of Physics, Indian Institute of Technology Ropar, Nangal Road, Rupnagar, Punjab, 140001, India

[2]Department of Chemistry, Science Laboratories, Durham University, Durham DH1 3LE, England, UK

* Corresponding author

† These authors have made equal contributions

ABSTRACT

The morphology of hydrophobic CF_4 plasma fluorinated polybutadiene surfaces has been characterised using atomic force microscopy (AFM). Judicious choice of the plasma power and exposure duration leads to formation of three different surface morphologies (Micro, Nano, and Micro+Nano). Scaling theory analysis shows that for all three surface topographies, there is an initial increase in roughness with length scale followed by a levelling-off to a saturation level. At length scales around 500 nm, it is found that the roughness is very similar for all three types of surfaces, and the saturation roughness value for the Micro+Nano morphology is found to be intermediate between those for the Micro and Nano surfaces. Fast Fourier Transform (FFT) analysis has shown that the Micro+Nano topography comprises a hierarchical superposition of Micro and Nano morphologies. Furthermore, the Micro+Nano surfaces display the highest local roughness (roughness exponent $\alpha = 0.42$ for length scales shorter than ~ 500 nm), which helps to explain their superhydrophobic behaviour (large water contact angle (> 170°) and low hysteresis (< 1°)).

1. INTRODUCTION

Length scales underpin many important areas of modern-day science and technology[1], with applications including the production of integrated circuits[2], information storage devices[3], display units[4], micro-electromechanical systems (MEMS)[5], miniaturized sensors[6], microfluidic devices[7], biochips[8], and photonic bandgap crystals[9]. For instance, the fundamental material properties of many useful size-dependent phenomena in optics, electronics, and magnetics displayed by nano-sized clusters of metals and semiconductors are governed by the length scales defining structure and organization[1]. In the case of solid surfaces, topographical roughness can strongly influence wettability, where the probe liquid can either penetrate into the surface structure or remain suspended on asperities creating air pockets underneath (commonly known as Wenzel[10] and Cassie-Baxter[11] states respectively). By utilising such roughened structures, it is possible to create superhydrophobicity (high water contact angles with low hysteresis[12]), which finds many technological applications including self-cleaning[13], rapid cooling[14], delayed freezing[15], crop spraying[16], and inkjet printing[17]. One of the most highly superhydrophobic surfaces reported to date is based on the CF_4 plasmachemical functionalisation and texturing of polybutadiene to create low surface energy (fluorinated) hierarchical roughness topographical structures[18, 19]. The impact and spreading of water droplets onto these surfaces has been shown to be strongly governed by the hierarchical surface topography (for similar overall surface chemical composition and roughness values)[20, 21].

In this article, the hierarchical surface topography which underpins superhydrophobicity for CF_4 plasma fluorinated polybutadiene surfaces is quantitatively analysed using scaling theory. Under this formalism, the variance of surface heights (h) from the mean (<h>) is measured over the sample surface. This variance, also termed as interface width or roughness (w), gives a measure of lateral correlations at the interface according to the equation:

$$w(r,t) = \left\langle \left(h(\vec{r},t) - \langle h(\vec{r},t) \rangle_{\vec{r}} \right)^2 \right\rangle_{\vec{r}}^{1/2} \qquad \text{Equation (1)}$$

where $\vec{r}$ is the position vector on the surface, t is the duration of surface modification, and $\langle\ \rangle_{\vec{r}}$ denotes the average over all $\vec{r}$ in a system of size L (where $r \leq L$)[22-24].

For short time scales and in the absence of any characteristic length present on the surface, the surface roughness follows a power law behaviour until a certain time after which the surface roughness saturates to a size dependent value $w_{sat}(L)$ whose finite size scaling defines the roughness exponent, α (which characterizes the roughness of the saturated interface) given by the

relation $w_{sat} \sim L^{\alpha}$. When α lies between 0 and 1, a smaller value of α corresponds to a rougher local surface, i.e., it signifies a more rapid change in surface heights[22]. In essence, this gives information on the localized jaggedness of a surface for a known root-mean-square (RMS) roughness. Saturation of the interface width is governed by height correlations developed across the surface, which means that sites across the surface are not completely independent, but depend upon the heights of neighbouring sites. Thus, the height fluctuations spread laterally with time. The characteristic length over which they are correlated is called the correlation length, ξ. On this basis, two surface heights are considered to be laterally correlated on average if their lateral separation is less than this correlation length. In other words, surface heights cease to be correlated beyond the lateral correlation length. At point of saturation the entire interface becomes correlated.

For the case of self-affine surfaces, the lateral correlation length is not a true characteristic length scale, but rather it is a relative length scale, since the magnitude of the lateral correlation length can be scaled to any arbitrary value[22]. In contrast, surfaces which do possess a characteristic length scale (i.e. non-self-affine) are called mounded surfaces, and for such surfaces, lateral correlation length (ξ) refers to the mound size, and the wavelength (λ) is the mound separation of the mounded surface[22, 25], Figure 1.

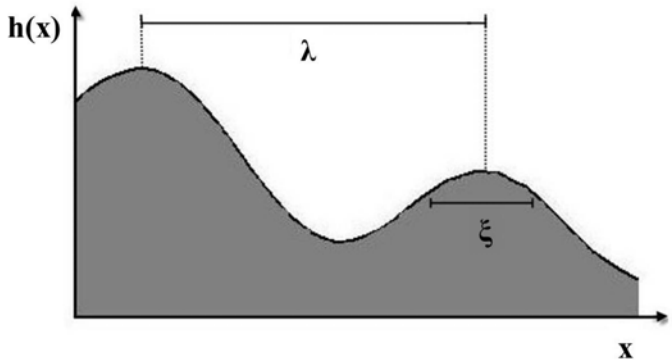

Figure 1: Lateral correlation length (ξ) and wavelength (λ) of a mounded surface[22]

Beyond the short range lateral height correlation of a surface, even though surface heights may not be significantly correlated, they can exhibit a periodic behavior at length scales exceeding the lateral correlation length (ξ). In order to determine this long-range behavior, the structure factor of the interfacial fluctuations (commonly referred to as power spectral density function (PSD)) should be taken into consideration. This is calculated by performing a Fourier transform of the 2-dimensional topographic data, and is defined as

$$PSD(k, t) = < H(k, t)H(-k, t)> \qquad \text{Equation (2)}$$

where H(k, t) is the Fourier transform of the surface height in a system size L, with k being the spatial frequency in reciprocal space[22, 26]. The spatial frequency corresponds to the lateral feature sizes, and the intensity of the distribution at each spatial frequency contains the average height information of the corresponding feature sizes. In the case of a surface possessing a characteristic length scale, a frequency peak is observed in the corresponding PSD spectrum. Surfaces that exhibit such characteristic length scales are said to be mounded. On the other hand, self-affine surfaces do not exhibit such length scales.

The above formalism can be applied to morphology studies of physically and chemically eroded surfaces[27-29]. In the case of superhydrophobic surfaces[30-33], important topographical parameters that characterize such surfaces include rms roughness (w(r,t)), in-plane correlation length (ξ), scaling exponents [34], power spectral density of the surface heights (PSD(k, t))[32], and Wenzel roughness parameter (ratio of the true surface area to the apparent surface area)[30]. Although it is well established that hierarchical surfaces can play a major role in superhydrophobicity[33, 35], scaling theory studies on such surfaces have not been reported. However, scaling theory has been used to study plasma deposited samples in the recent past [36-38].

2. EXPERIMENTAL

2.1 Sample Preparation

Polybutadiene (Sigma-Aldrich Inc., M_w = 420,000, 36% cis 1,4 addition, 55% trans 1,4 addition, 9% 1,2 addition) dissolved in toluene (BDH, +99.5% purity) at a concentration of 5% (w/v) was spin coated onto polished silicon (100) wafers (Silicon Valley Microelectronics Inc.) using a photoresist spinner (Cammax Precima) operating at 3000 rpm. These polymer films were subsequently annealed at 90 °C under vacuum for 60 min to remove entrapped solvent.

CF_4 plasma fluorination was carried out in a cylindrical glass reactor (5 cm diameter, 470 cm^3 volume) enclosed in a Faraday cage[39]. This was connected to a two stage rotary pump via a liquid nitrogen cold trap with a base pressure of 2 x 10^{-3} mbar and a leak rate better than 6 x 10^{-9} mol s^{-1}. An inductor-capacitor (L-C) impedance matching unit was used to minimise the standing wave ratio (SWR) for the power transmitted from a 13.56 MHz radio frequency generator to a copper coil externally wound around the glass reactor. Prior to each plasma treatment, the chamber was scrubbed with detergent, rinsed in propan-2-ol, and further cleaned using a 50 W air plasma for

30 min. A piece of polybutadiene coated substrate was then placed into the centre of the reactor, followed by evacuation to base pressure. Next, CF_4 gas (99.7% purity, Air Products) was admitted into the system via a needle valve at a pressure of 0.2 mbar, and the electrical discharge ignited. Upon completion of plasma treatment, the gas feed was turned off, and the chamber vented to atmosphere. Three different types of plasmachemical textured surfaces were prepared by varying the process parameters (see Table 1). For each, the surface XPS F:C ratio remained constant[18, 20].

Table 1: CF_4 plasmachemical texturing process parameters and corresponding water contact angle measurements.

Surface Texture	**CF_4 Plasma**		**Contact Angle**	
	Power (W)	**Duration (min)**	**Static (°)**	**Hysteresis (°)**
Micro	30	5	164±2	8±1
Nano	60	5	167±2	4±1
Micro+Nano	30	10	>170	<1

2.2 Surface Characterisation

Microlitre sessile drop contact angle analysis was carried out with a video capture system (VCA2500XE, AST Products Inc.) using a 1.0 μL dispensation of de-ionised water (BS 3978 grade 1). Static contact angle measurement was taken after 10 s and no visible change was observed during this period. Contact angle hysteresis values were calculated from the difference between advancing and receding angles, which were measured by respectively increasing and decreasing the droplet size until the contact line was observed to move[40]. Our previous studies have shown that picolitre droplets result in bouncing off the CF_4 plasmachemical textured surfaces, and therefore microlitre droplets were employed in the current study[20].

AFM images (512×512 lines) were acquired using a scanning probe microscope (Digital Instruments Nanoscope III). Damage to the tip and sample surface was minimised by employing Tapping Mode AFM (tip spring constant = 40 Nm^{-1}; tip radius = 8 nm; tip height = 17.5 μm; front angle = 15°; back angle =25°; side angle = 17.5°). Assignment of the sample names in Table 1 was

carried out on the basis of the surface morphology observed in the AFM images. For each sample type, nine 25 μm x 25 μm images were recorded from different locations across the surface.

2.3 AFM Image Analysis

In order to further characterise the three different surface morphologies, scaling theory analyses were performed. Specifically, the interface width (w, commonly known as the surface roughness) was studied as a function of length scale (L). For a particular AFM image, a Fortran program utilizing equation (1) extracted interface widths for all possible square areas within the image. Next, the obtained interface widths were averaged for identical square areas (each area corresponding to a particular length scale) and then used for plotting interface width (w) versus length scale (L) graphs. For each sample surface, at least 9 images from different regions were analysed and subsequently averaged to give respective interface width versus length scale plots. These were used to calculate roughness exponents (α) using the relation $w_{sat} \sim L^{\alpha}$ by fitting the linear portions of log(w) versus log(L) curves to a scaling power law.

WSxM software was used for Fast Fourier Transform (FFT) filtering analyses on the acquired AFM images and also to determine saturation roughness values[41]. For the Micro+Nano surface, the individual Micro and Nano contributions towards the overall Micro+Nano morphology were extracted by applying an appropriate band pass filter to separate out the respective low/high frequencies corresponding to the longer/shorter length scales. Thereafter, a reverse Fourier transformation was performed utilising only these individual low/high frequency filtered components in order to reconstruct the respective Micro/Nano topographical features of the overall Micro+Nano surface.

Power spectral density (PSD) analyses were also obtained from the corresponding FFT images using WSxM software[41]. The FWHM (Full Width at Half Maximum) of each PSD curve was taken as being inversely proportional to the lateral correlation length (ξ) i.e., mound size; whilst the peak position of the PSD curve provided a measure of the inverse mound separation (λ^{-1}) [22].

3. RESULTS AND DISCUSSION

3.1 AFM Surface Topography

The CF_4 plasmachemical textured Micro surface displays a large scale lamellar morphology, whilst small nanometer-sized hemisphere-like structures are clearly discernible for the Nano surface,

Figure 2. In the case of the Micro+Nano sample, lamellar structures with superimposed nanometer sized structures are visible. These differences in surface topography are understood to stem from the interaction between the CF_4 plasma and the polybutadiene surface[18]. This entails the applied alternating RF electromagnetic field across the CF_4 plasma leading to electron acceleration, and culminating in fragmentation and ionization of CF_4 gas molecules. Surface roughening occurs as a consequence of volatile, low molecular weight species being formed during polymer chain cleavage by ion bombardment[42], vacuum ultraviolet (VUV) irradiation[43], and chemical attack by fluorine atoms. Such polymer chain scission enhances surface mobility culminating in topographical rearrangement[44, 45] so as to minimise the surface free energy[46, 47]. The extent of this polymer chain rearrangement and etching gives rise to the observed range of surface topographies (i.e. by varying parameters such as plasma power and exposure time during plasma processing)[18, 20, 48]. Also, VUV irradiation penetrates below the polymer film surface[49] to cause dissociation of polymer chain σ-bonds[50], and facilitating cross-linking of the subsurface through reaction with unsaturated polybutadiene carbon-carbon double bonds to create regions more resilient towards ablation (surface roughness)[51]. VUV irradiation however does not affect the bulk properties of the polymer because the penetration depth is typically less than 100 nm[50-52].

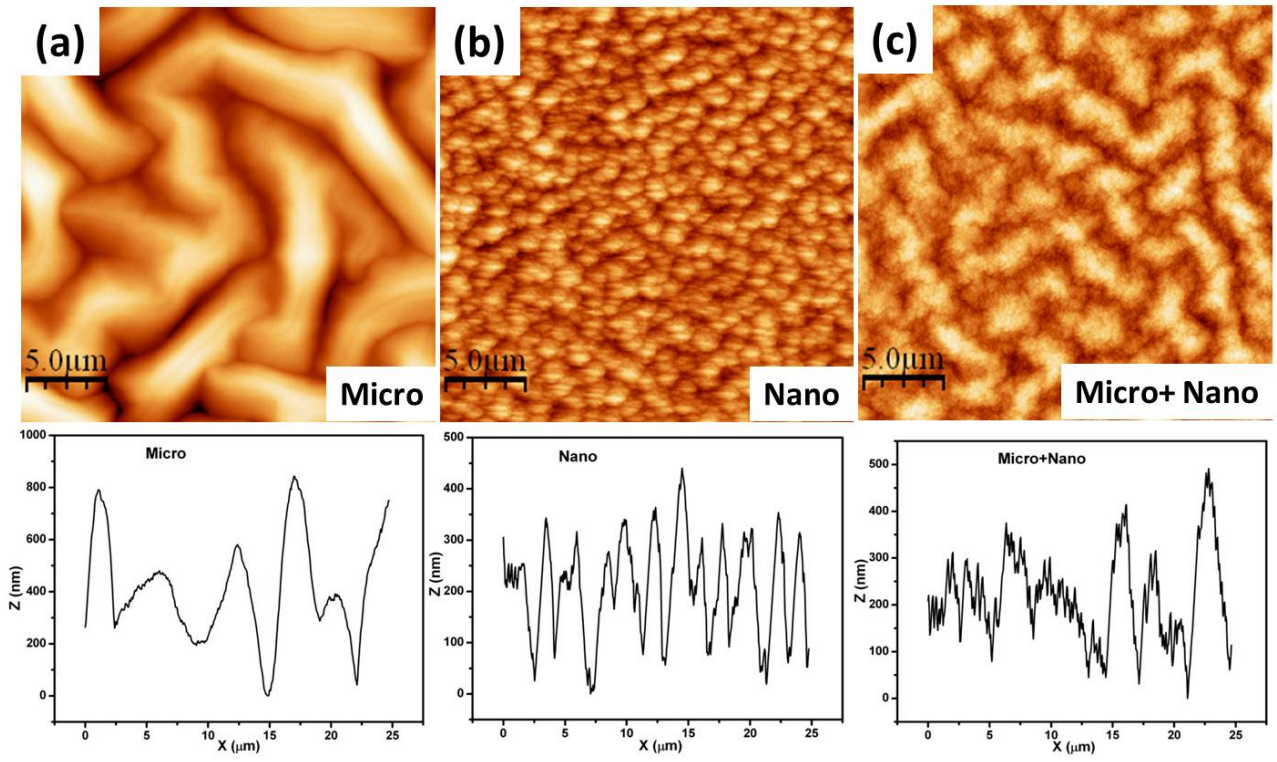

Figure 2. 25×25 μm AFM images and their corresponding representative line profiles of (a) Micro, (b) Nano, and (c) Micro+Nano surfaces.

In the present study, large scale undulating features (designated as Micro surfaces) are formed on the surface at low powers (30 W, 5 min) which can be attributed to a small degree of polymer chain scission, Figure 2. These large scale features diminish at higher power levels (60 W, 5 min) to be replaced by finer scale roughness features (designated as Nano surfaces) as a consequence of greater polymer chain scission and surface ion bombardment. However, at low power (30 W) but longer CF_4 plasma exposure time (10 min), a hybrid microscale lamellar morphology with nanometer sized structures is created (designated Micro + Nano) due to the longer plasma exposure time causing more chain scission and surface ion bombardment compared to the Micro morphology.

3.2 Length Scale Analysis of Surface Roughness

Figure 3 shows a typical graph for a Micro+Nano surface in which roughness (interface width, w) versus length scale (L) curves for nine different images are plotted together with their average. A similar methodology was employed to extract corresponding topographical parameters from the Micro and Nano surface AFM images.

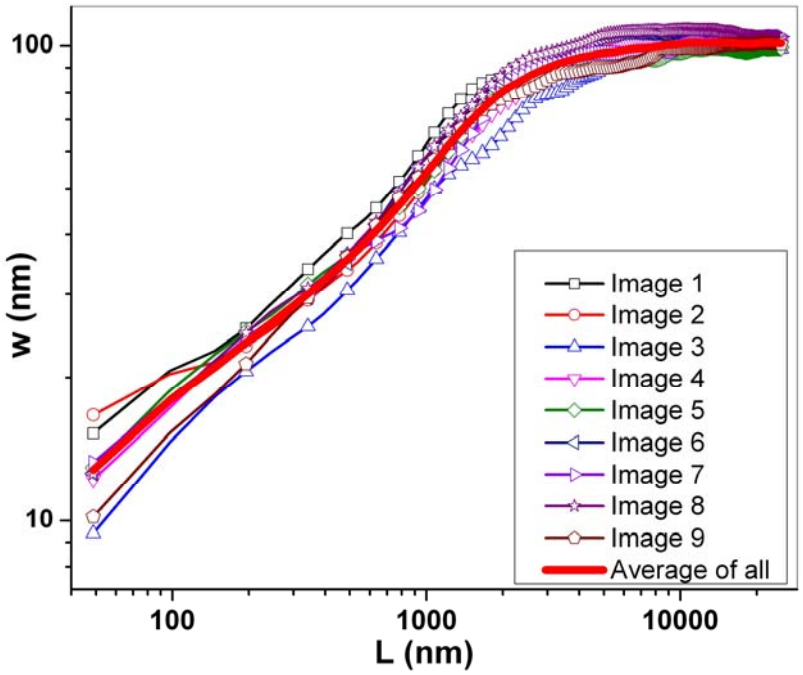

Figure 3. Plot of interface width (w) versus length scale (L) for 9 images acquired from different regions of a single Micro+Nano surface, and also their average.

Figure 4 displays the variation of interface widths (w) for all three surface types with respect

to length scale (L). The plot shows that there is an initial increase in roughness with length scale which is followed by saturation for all three morphology types. This roughness plateau occurs at length scales larger than L ~ 2000 nm, and the roughness is greatest for the Micro surface (w ~ 220 nm) and lowest for the Nano surface (w~ 90 nm), and in fact corroborates well to the respective large and fine scale features observed on the Micro and Nano surfaces, Table 2. Furthermore, the saturation roughness for the Micro+Nano surface fits in well between the Micro and Nano surface plots.

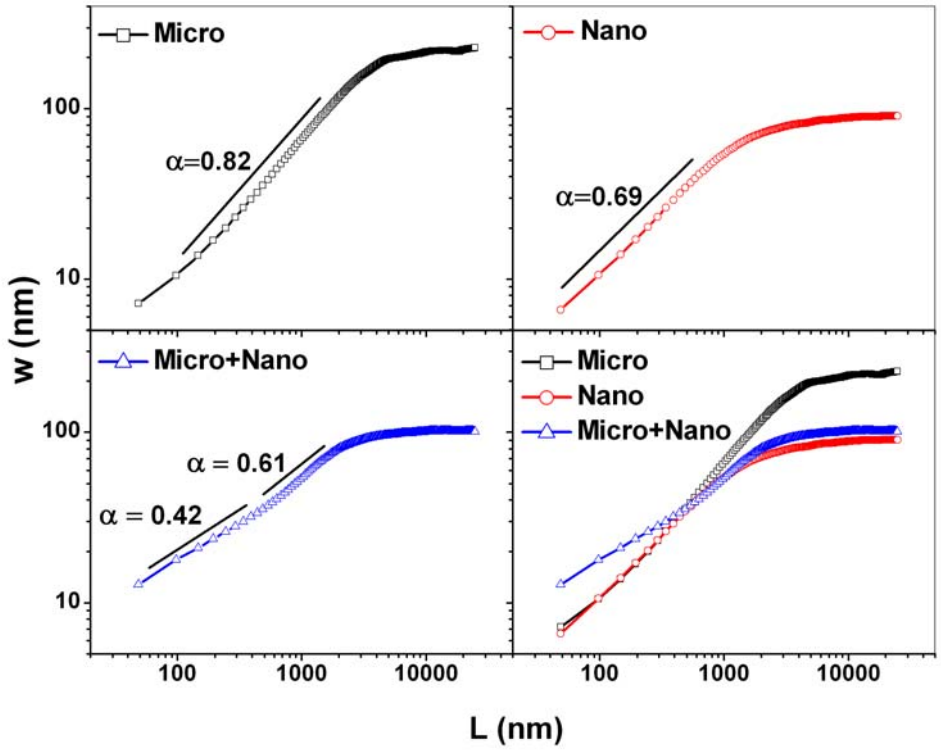

Figure 4. Plots of interface width (w) versus length scale (L) curves for the Micro, Nano, and Micro+Nano surfaces. The slopes of the straight lines illustrated adjacent to the linear portions of each graph were used to calculate their respective roughness exponent (α) values. Error in calculation of α is included in Table 2.

Table 2: Saturation roughness, and roughness exponents (α) calculated for Micro, Nano and Micro+Nano surfaces.

Surface Texture	**Length Scale Analysis**	
	Saturation Roughness (nm)	**Roughness Exponent (α-value)**

Micro	220±30	0.82±0.00335
Nano	90±8	0.69±0.00723
Micro+Nano	100±6	0.42±0.00472 and 0.61±0.00417

The roughness (interface width, w) versus length scale (L) curves for the Micro and Nano surfaces coincide over shorter length scales, Figure 4. This could be due to the fact that the average widths as well as the height profiles of the respective lamellar and fine structures at shorter length scales have very similar values, thereby yielding nearly identical roughness values. Furthermore, compared to the respective Micro and Nano topographies, the Micro+Nano surface displays a greater roughness over short length scales (i.e., less than L ~ 500 nm) and correlates to greater hydrophobicity. Whilst at longer length scales, the Micro+Nano roughness values are quite close to the Nano surface. Finally, it is of interest to note that at a length scale of approximately 500 nm, the roughnesses for all three surface types are very similar.

Roughness exponent values (α) were obtained from slopes of the interface width (w) versus length scale (L) plots, with the highest value found for the Micro surface (α = 0.82), and the smallest for the Micro+Nano surface, Figure 4 and Table 2. At very short length scales (~ 100 nm), there are only two points for the Micro surface, and so they cannot be considered as a region of different slope – in fact it can be clearly seen that there is a single linear fit for the Micro surface across the same length scale range for which there are 2 linear fits for the Micro+Nano surface. The higher α value for the Micro surface suggests that it is locally smoother in comparison to the Micro+Nano surface[22]. Whilst the Nano surface has an intermediate local roughness (α = 0.69). Interestingly, only a single α value was found for each of the Micro and Nano surfaces, whereas two α values (0.42 and 0.61) were obtained for the Micro+Nano surface (this was done by slightly changing and shifting the region of linear fitting until the best fit was achieved). For the latter, the α value crossover point occurred at an approximate length scale of 500 nm, thus implying locally rough (low α value ~ 0.42) and smooth (high α value ~ 0.61) morphologies at length scales (L) less than and greater than 500 nm respectively.

3.3 Fast Fourier Transform Analysis of Surface Roughness

In order to separate out the roughness scales for the Micro+Nano surface, Fast Fourier Transform filtering analysis was performed on a representative AFM image, Figure 5. Using this approach, the average saturation roughness values for the Micro and Nano components were found to be 70.2 nm and 43.4 nm respectively. The summation of these values (113.6 nm) for this specific AFM image

matches well with the average saturation roughness value of 108 nm obtained across all regions examined of the same representative Micro+Nano surface, Table 2.

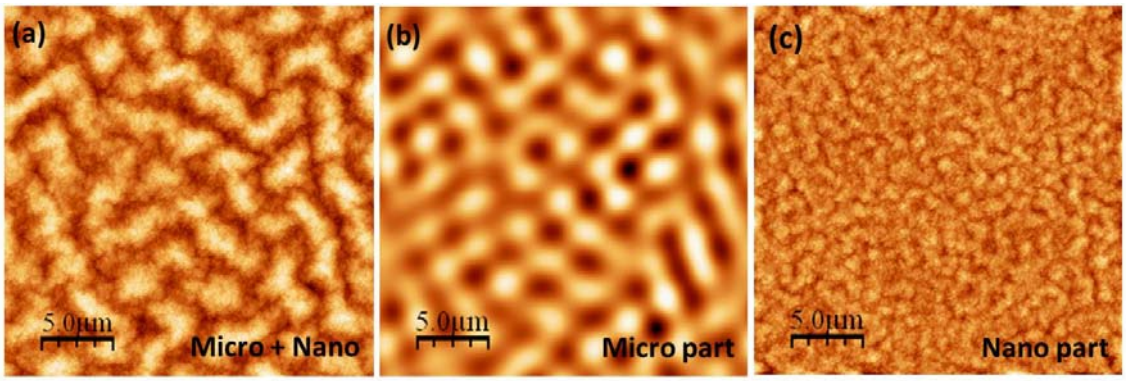

Figure 5. (a) Raw Micro+Nano AFM image; (b) Micro component obtained from Fast Fourier Transform filter analysis; and (c) Nano component obtained from Fast Fourier Transform filter analysis.

3.4 Power Spectral Density (PSD) Analysis of Surfaces

Power spectral density (PSD) analyses performed on the AFM images display a distinct frequency peak in the PSD spectra for the Micro+Nano surface which confirms that the surface is mounded, Figure 6. For the Nano surface, the characteristic frequency peak is not as definitive as for the Micro+Nano surface, which suggests that repetition of the characteristic length scale is not as well defined as for the Micro+Nano surface. This is consistent with the mounds not being as clear in the Nano surface AFM images as they are for the Micro+Nano surface, Figure 2. The PSD spectra of the Micro surface shows a broad peak which corresponds to its large surface features.

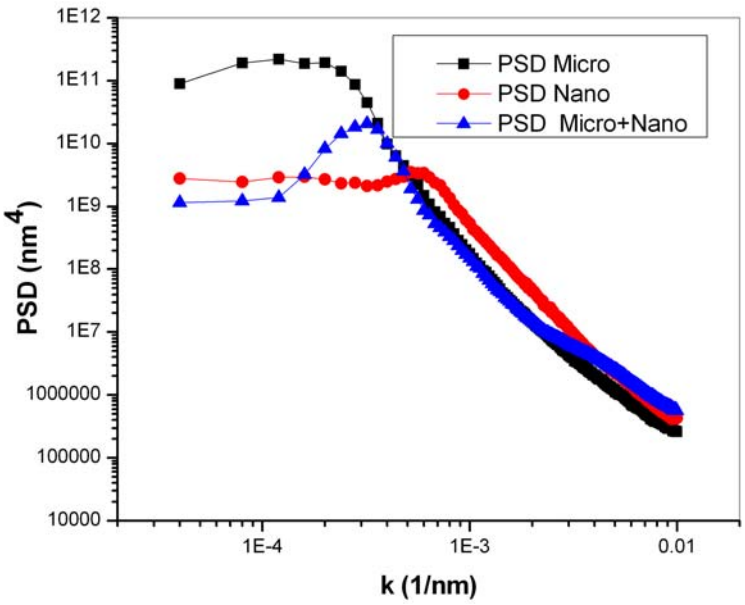

Figure 6. Averaged Power Spectral Density (PSD) analysis of Micro, Nano, and Micro+Nano

surfaces.

Mound size 'ξ' and mound separation 'λ' were calculated from the PSDs for each of the different morphologies[28], Figure 7. It was found that the Micro surface exhibits an intermediate mound size but the largest mound separation. It should be borne in mind that the mound size and separation estimated using this method correspond to the radial average sizes for each image.

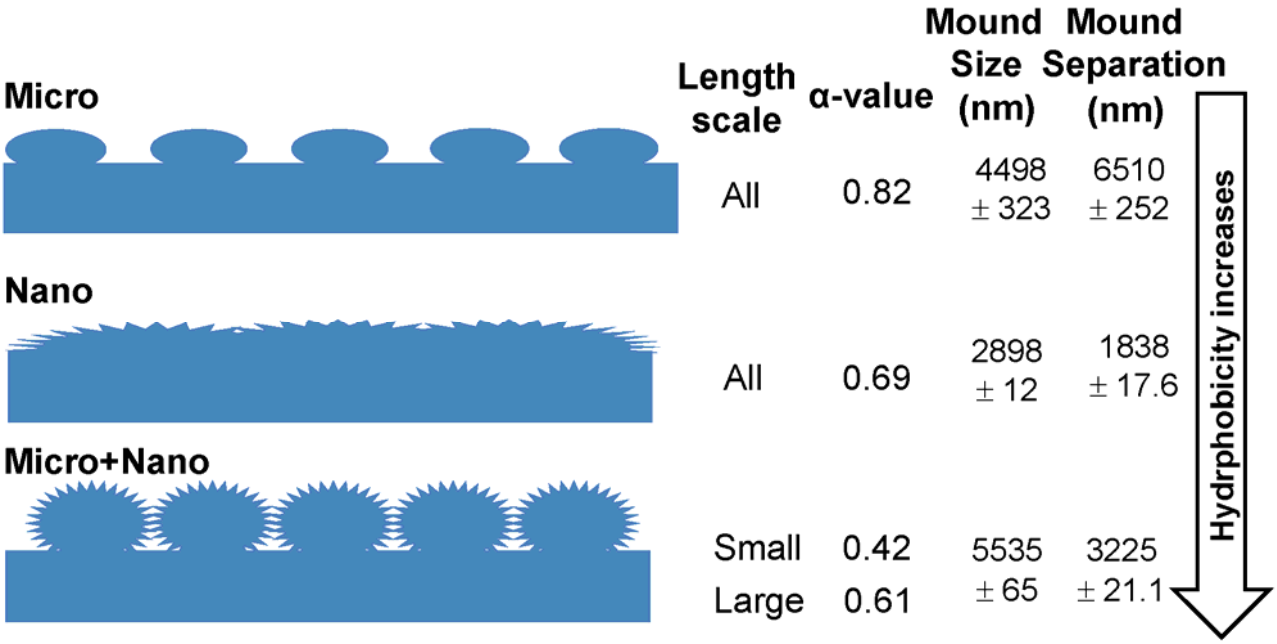

Figure 7. The surface roughness exponent (α) values were obtained from length scale analysis (Table 2) and the mound sizes/separations from power spectral density (PSD) analyses.

3.5 Hierarchical Superhydrophobicity

Contact angle analysis (in particular contact angle hysteresis) has shown that the Nano surface is more hydrophobic than the Micro surface[20], Table 1. This can be explained in terms of the roughness exponent parameter being the largest (smoothest) for the Micro surface ($\alpha \sim 0.82$), followed by the Nano surface ($\alpha \sim 0.69$) and then the Micro+Nano surface (two α values: 0.42 and 0.61). This overall ranking of the roughness exponent values corresponds to the Micro surface being the smoothest, followed by the Nano surface with greater roughness compared to the Micro surface over similar length scales, and the Micro+Nano surface having the highest local roughness amongst all three surfaces. Furthermore, the latter has been shown to be relatively rougher at length scales shorter than $L \sim 500$ nm and relatively smoother (but rougher compared to the other surfaces) above this length scale. These two hierarchical length scales of surface roughness for the Micro+Nano surface provide the greatest superhydrophobicity (high contact angles and low hysteresis) due to formation of the Cassie−Baxter state[35, 53-55], Table 1.

4. CONCLUSION

Hierarchically structured superhydrophobic CF_4 plasma fluorinated polybutadiene surfaces have been characterized using scaling theory. The surface topography can be altered by varying the plasma power and exposure time. Three types of (super)hydrophobic morphologies have been examined – Micro, Nano, and Micro+Nano. For short length scales, the Micro surface is smoothest, followed by the Nano topography, and roughest for the Micro+Nano surface. Whilst, for larger length scales, the Micro surface is the roughest, followed by Micro+Nano, and the Nano surface is smoothest. Although all three morphologies are hydrophobic (contact angles > 160^o), only the composite (Micro+Nano) surface displays low contact-angle hysteresis thus making it superhydrophobic. This fits in well with superhydrophobic surfaces requiring microscale trough widths (mound separation) as well as hierarchical length scales (two different values of the roughness exponents (α) in the present case of Micro+Nano surface)[35]_ENREF_35.

5. ACKNOWLEDGEMENTS

Engineering and Physical Sciences Research Council (EPSRC) grant reference numbers EP/H018913/1 and EP/J005401/1.

6. REFERENCES

1. Geissler, M. and Y. Xia, *Patterning: Principles and some new developments.* Advanced Materials, 2004. **16**(15): p. 1249-1269.
2. Thompson, S.E., et al., *In search of "forever," continued transistor scaling one new material at a time.* IEEE Transactions on Semiconductor Manufacturing, 2005. **18**(1): p. 26-35.
3. Lister, S.J., et al., *Size-dependent reversal of grains in perpendicular magnetic recording media measured by small-angle polarized neutron scattering.* Applied Physics Letters, 2010. **97**(11): p. 112503-3.
4. Hung, C.P., W.G. Liu, and Y.C. Hsu, *Rotating RGB LED true-color displayer design and control method.* International Journal of Innovative Computing, Information and Control, 2013. **9**(2): p. 679-692.
5. Mehmet, Y. and W.K. Jeffrey, *Monolithic integration of nanoscale tensile specimens and MEMS structures.* Nanotechnology, 2013. **24**(16): p. 165502.
6. Jürgen, C., *A miniaturized dual-fibre laser Doppler sensor.* Measurement Science and Technology, 2001. **12**(8): p. 1191-1198.
7. Lei, K.F., *Recent developments and patents on biological sensing using nanoparticles in microfluidic systems.* Recent Patents on Nanotechnology, 2013. **7**(1): p. 81-90.
8. Singh, R.P., et al., *Smart nanomaterials for biosensors, biochips and molecular bioelectronics*, in *Smart Nanomaterials for Sensor Application*, L. Songjun, G. Yi, and L. He, Editors. 2012, Bentham Science Publishers. p. 3-41.
9. Song, H.W., *Self-assembly of lanthanide oxide photonic crystals and its modification on spontaneous emission.* Chinese Journal of Luminescence, 2013. **34**(1): p. 1-11.
10. Wenzel, R.N., *Resistance of solid surfaces to wetting by water.* Industrial & Engineering Chemistry, 1936. **28**(8): p. 988-994.
11. Cassie, A.B.D. and S. Baxter, *Wettability of porous surfaces.* Transactions of the Faraday Society, 1944. **40**: p. 546-551.
12. Öner, D. and T.J. McCarthy, *Ultrahydrophobic surfaces: Effects of topography length scales on wettability.* Langmuir, 2000. **16**(20): p. 7777-7782.
13. Barthlott, W. and C. Neinhuis, *Purity of the sacred lotus, or escape from contamination in biological surfaces.* Planta, 1997. **202**(1): p. 1-8.

14. Yao, S.C. and K.J. Choit, *Heat transfer experiments of mono-dispersed vertically impacting sprays.* International Journal of Multiphase Flow, 1987. **13**(5): p. 639-648.
15. Tourkine, P., M. Le Merrer, and D. Quéré, *Delayed freezing on water repellent materials.* Langmuir, 2009. **25**(13): p. 7214-7216.
16. Reichard, D.L., *Drop formation and impaction on the plant.* Weed Technology, 1988. **2**(1): p. 82-87.
17. Calvert, P., *Inkjet printing for materials and devices.* Chemistry of Materials, 2001. **13**(10): p. 3299-3305.
18. Woodward, I., et al., *Super-hydrophobic surfaces produced by plasma fluorination of polybutadiene films.* Langmuir, 2003. **19**(8): p. 3432-3438.
19. Woodward, I.S., et al., *Micropatterning of plasma fluorinated super-hydrophobic surfaces.* Plasma Chemistry and Plasma Processing, 2006. **26**(5): p. 507-516.
20. Brown, P.S., et al., *Impact of picoliter droplets on superhydrophobic surfaces with ultralow spreading ratios.* Langmuir, 2011. **27**(22): p. 13897-13903.
21. Brown, P.S., et al., *Superhydrophobic hierarchical honeycomb surfaces.* Langmuir, 2012. **28**(38): p. 13712-13719.
22. Pelliccione, M. and T.M. Lu, *Evolution of thin film morphology: Modeling and simulations*. Springer Series in Materials Science, ed. H. Robert, et al. 2008, Berlin: Springer.
23. Family, F. and T. Vicsek, *Dynamics of fractal surfaces*. 1991, Singapore: World Scientific Pub. Co. Inc.
24. Auger, M.A., et al., *Growth dynamics of reactive-sputtering-deposited AlN films.* J. Appl. Phys., 2005. **97**: p. 123528.
25. Pelliccione, M., et al., *Mound formation in surface growth under shadowing.* Physical Review B, 2006. **74**(12): p. 125420.
26. Dhillon, P.K., et al., *Si nanoripples: A growth dynamical study.* Applied Surface Science, 2012. **258**(24): p. 9579-9583.
27. Buijnsters, J.G., M. Camero, and L. Vázquez, *Growth dynamics of ultrasmooth hydrogenated amorphous carbon films.* Physical Review B, 2006. **74**(15): p. 155417.
28. Pelliccione, M., T. Karabacak, and T.M. Lu, *Breakdown of dynamic scaling in surface growth under shadowing.* Physical Review Letters, 2006. **96**(14): p. 146105.
29. Cafiero, R., V. Loreto, and P.P. Prosini, *Anisotropy and non-universality in kinetic roughening.* Europhys. Lett., 1998. **42**(4): p. 389-394.

30. David, R. and A. Wilhelm Neumann, *Computation of the wetting properties of randomly structured superhydrophobic surfaces.* J. Phys. Chem. C, 2012. **116**: p. 16601-16608.
31. Yang, C., U. Tartaglino, and B.N.J. Persson, *Influence of surface roughness on superhydrophobicity.* Physical Review Letters, 2006. **97**(11): p. 116103.
32. Awada, H., et al., *Correlation between Superhydrophobicity and the Power Spectral Density of Randomly Rough Surfaces.* Langmuir, 2010. **26**(23): p. 17798-17803.
33. Bottiglione, F. and G. Carbone, *Role of statistical properties of randomly rough surfaces in controlling superhydrophobicity.* Langmuir, 2013. **29**(2): p. 599-609.
34. Sarkar, S., et al., *Effect of self-affine fractal characteristics of surfaces on wetting.* Applied Physics Letters, 2010. **96**(6): p. 063112-3.
35. Li, W. and A. Amirfazli, *Hierarchical structures for natural superhydrophobic surfaces.* Soft Matter, 2008. **4**(3): p. 462-466.
36. Álvarez, R., et al., *Morphological evolution of pulsed laser deposited ZrO2 thin films.* J. Appl. Phys., 2010. **107**: p. 1-10.
37. Alvarez, R., et al., *Atomistic model of ultra-smooth amorphous thin film growth by low-energy ion-assisted physical vapour deposition.* J. Phys. D: Appl. Phys., 2013. **46**(39): p. 395303.
38. Terriza, A., et al., *Roughness assessment and wetting behavior of fluorocarbon surfaces.* Journal of Colloid and Interface Science, 2012. **376**(1): p. 274-282.
39. Hynes, A.M., M.J. Shenton, and J.P.S. Badyal, *Plasma polymerization of trifluoromethyl-substituted perfluorocyclohexane monomers.* Macromolecules, 1996. **29**(1): p. 18-21.
40. Johnson, R.E.J. and R.H. Dettre, *Wetting of low energy surfaces*, in *Wettability*, J.C. Berg, Editor. 1993, Marcel Dekker: New York. p. 1-74.
41. Horcas, I., et al., *WSxM: A software for scanning probe microscopy and a tool for nanotechnology.* Rev. Sci. Instrum., 2007. **78**: p. 013705.
42. Yasuda, H., *Plasma polymerization*. 1985, New York: Academic Press.
43. Egitto, F.D., *Plasma etching and modification of organic polymers.* Pure and Appl. Chem., 1990. **62**(9): p. 10.
44. Poncin-Epaillard, F., J.C. Brosse, and T. Falher, *Cold plasma treatment: Surface or bulk modification of polymer films?* Macromolecules, 1997. **30**(15): p. 4415-4420.
45. Boyd, R.D., et al., *Atmospheric nonequilibrium plasma treatment of biaxially oriented polypropylene.* Macromolecules, 1997. **30**(18): p. 5429-5436.

46. Andrade, J.D., *Polymer surface dynamics*. 1988, Berlin: Springer.
47. Occhiello, E., et al., *Oxygen-plasma-treated polypropylene interfaces with air, water, and epoxy resins: Part I. Air and water.* Journal of Applied Polymer Science, 1991. **42**(2): p. 551-559.
48. Kogelschatz, U., et al., *High-intensity sources of incoherent UV and VUV excimer radiation for low-temperature materials processing.* Special Issue: Proceedings of the European Materials Research, 2000. **168**(1–4): p. 29-36.
49. Clark, D.T. and A. Dilks, *ESCA applied to polymers. XVIII. RF glow discharge modification of polymers in helium, neon, argon, and krypton.* Journal of Polymer Science: Polymer Chemistry Edition, 1978. **16**(5): p. 911-936.
50. Holländer, A., R. Wilken, and J. Behnisch, *Subsurface chemistry in the plasma treatment of polymers.* Surface and Coatings Technology, 1999. **116–119**: p. 788-791.
51. Liston, E.M., L. Martinu, and M.R. Wertheimer, *Plasma surface modification of polymers for improved adhesion: a critical review.* Journal of Adhesion Science and Technology, 1993. **7**(10): p. 1091-1127.
52. Poncin-Epaillard, F., B. Chevet, and J.-C. Brosse, *Modification of isotactic poly(propylene) with a nitrogen plasma; differences in comparison to the treatment with a carbon dioxide plasma.* Die Makromolekulare Chemie, 1991. **192**(7): p. 1589-1599.
53. Bico, J., C. Marzolin, and D. Quéré, *Pearl drops.* EPL (Europhysics Letters), 1999. **47**(2): p. 220.
54. Luo, B.H., et al., *Surface geometrical model modification and contact angle prediction for the laser patterned steel surface.* Surface and Coatings Technology, 2010. **205**(7): p. 2597-2604.
55. Tuteja, A., et al., *Design parameters for superhydrophobicity and superoleophobicity.* MRS Bulletin, 2008. **33**: p. 752-758.